

# Spectroscopic and theoretical studies on the structural, electronic, and optical properties of zinc octaethylporphyrin/C<sub>60</sub> co-deposited films

Jun Onoe, Shinta Watanabe, Shiro Kato, Masato Nakaya, and Jean-Pierre Bucher

Citation: *The Journal of Chemical Physics* **147**, 214701 (2017); doi: 10.1063/1.5005068

View online: <https://doi.org/10.1063/1.5005068>

View Table of Contents: <http://aip.scitation.org/toc/jcp/147/21>

Published by the [American Institute of Physics](#)

---

## Articles you may be interested in

[Communication: Mechanochemical fluctuation theorem and thermodynamics of self-phoretic motors](#)

*The Journal of Chemical Physics* **147**, 211101 (2017); 10.1063/1.5008562

[Detailed balance, internal consistency, and energy conservation in fragment orbital-based surface hopping](#)

*The Journal of Chemical Physics* **147**, 214113 (2017); 10.1063/1.5003820

[Nuclear spin/parity dependent spectroscopy and predissociation dynamics in  \$\nu\_{OH} = 2 - 0\$  overtone excited Ne-H<sub>2</sub>O clusters: Theory and experiment](#)

*The Journal of Chemical Physics* **147**, 214304 (2017); 10.1063/1.5001335

[Orientation dependence of the work function for metal nanocrystals](#)

*The Journal of Chemical Physics* **147**, 214301 (2017); 10.1063/1.4991725

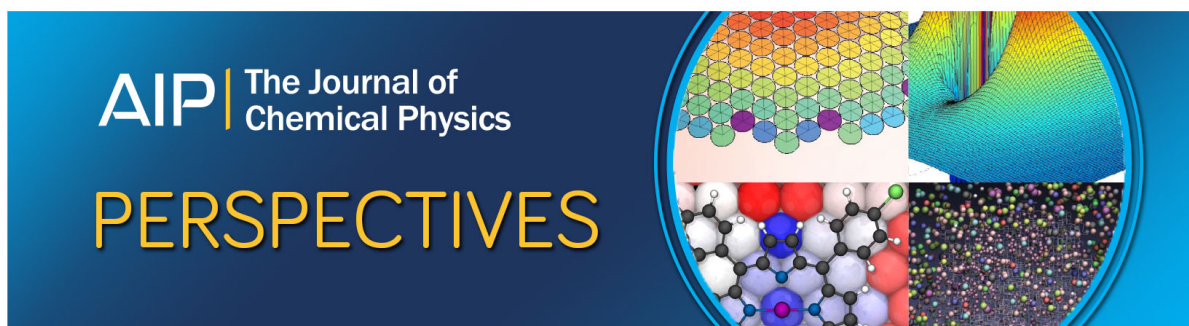
[Optimizing the formation of colloidal compounds with components of different shapes](#)

*The Journal of Chemical Physics* **147**, 214501 (2017); 10.1063/1.5006047

[Analytical energy gradients for explicitly correlated wave functions. I. Explicitly correlated second-order Møller-Plesset perturbation theory](#)

*The Journal of Chemical Physics* **147**, 214101 (2017); 10.1063/1.5003065

---



# Spectroscopic and theoretical studies on the structural, electronic, and optical properties of zinc octaethylporphyrin/C<sub>60</sub> co-deposited films

Jun Onoe,<sup>1,a)</sup> Shinta Watanabe,<sup>1</sup> Shiro Kato,<sup>1</sup> Masato Nakaya,<sup>1</sup> and Jean-Pierre Bucher<sup>2</sup>

<sup>1</sup>Department of Energy Science and Engineering, Nagoya University, Furo-cho, Chikusa-ku, Nagoya 464-8603, Japan

<sup>2</sup>Université de Strasbourg, CNRS, IPCMS UMR 7504, F-67034 Strasbourg, France

(Received 16 September 2017; accepted 8 November 2017; published online 1 December 2017)

We have examined the structural, electronic, and optical properties of zinc-octaethylporphyrin [Zn(OEP)]/C<sub>60</sub> co-deposited films to elucidate the donor (D)–acceptor (A) interactions at the D/A interface of heterojunction organic solar cells (OSCs), using Fourier-transform infrared (FT-IR) spectroscopy, X-ray diffraction (XRD), ultraviolet-visible (UV–vis) spectroscopy, and photoluminescence (PL) spectroscopy in combination with first-principles and semi-empirical calculations. The FT-IR and XRD results indicated that Zn(OEP) and C<sub>60</sub> were mixed with each other at the molecular level in the co-deposited film. The theoretical calculations suggested that in the interfacial region, it is energetically preferable for the C<sub>60</sub> molecule to face the center of the planar structure of Zn(OEP) at a distance of 2.8 Å rather than the edge of the structure at a distance of 5.0 Å. After consideration of the C<sub>60</sub> solvent effects, this coordination model for C<sub>60</sub>–Zn(OEP) adequately explained the line shift of the UV–vis peaks with respect to the proportion of C<sub>60</sub> in the co-deposited films. A comparison of the energy level diagrams of Zn(OEP) before and after the interaction with C<sub>60</sub> revealed that the LUMO, HOMO, and HOMO-1 were significantly affected by the interaction with C<sub>60</sub>. In particular, the HOMO-1 wave function became spread over a portion of C<sub>60</sub>, although the charge transfer between Zn(OEP) and C<sub>60</sub> was almost negligible. Since no PL peaks (S<sub>1</sub> → S<sub>0</sub>) from the excited Soret band of Zn(OEP) were observed for the Zn(OEP)/C<sub>60</sub> co-deposited films, the D/A mixing layers played a crucial role in completely dissolving the photogenerated excitons to electrons-hole pairs that cause the short-circuit current, which is relevant to improving the energy conversion efficiency of OSCs. *Published by AIP Publishing.* <https://doi.org/10.1063/1.5005068>

## I. INTRODUCTION

Energy-harvesting devices have attracted a great deal of attention and are expected to play a key role in the development of a sustainable society. In particular, organic solar cells (OSCs) have been extensively investigated by researchers around the world working on the next-generation solar cells, owing to their fascinating advantages of low weight, reduced fabrication cost, sustainability, and flexibility when compared to conventional solar cells based on silicon (Si) and semiconductor compounds (SCs).<sup>1,2</sup> However, OSCs exhibit energy conversion efficiencies ( $\eta$ ) of ca. 10% at most,<sup>3</sup> which is still much lower than those for the conventional Si ( $\eta_{\max}$ : ca. 25%) and SC ( $\eta_{\max}$ : ca. 40%) solar cells.<sup>4</sup> To further improve the  $\eta$  of OSCs, it is essential to understand both the fundamental mechanisms that determine the photoconversion current, which influences the short-circuit current, and those that determine the open-circuit voltage, by examining OSCs with well-defined structures.<sup>5</sup>

Figure 1 schematically illustrates OSCs with the representative structures of (a) double heterojunction,<sup>6</sup> (b) bulk heterojunction,<sup>7</sup> and (c) comb-type heterojunction.<sup>8</sup> Here, indium tin oxide (ITO) and metals such as aluminum (Al) are often used as the cathode and anode materials, respectively. The complex structure of bulk heterojunctions makes it difficult to understand the reason behind any improvements in  $\eta$  because it is challenging to reproduce or even precisely characterize the junction structure. In contrast, comb-type heterojunctions are basically regarded as multiple double heterojunctions with lateral contacts to both electrodes. Hence, in the present study, OSCs with the well-defined double-heterojunction structure consisting of donor (D) and acceptor (A) films were examined.

Figure 2 schematically illustrates the double-heterojunction OSC (left side) investigated in the present study. We used zinc octaethylporphyrin [Zn(OEP)] and C<sub>60</sub> as the donor and acceptor, respectively, and ITO and Al as the cathode and anode, respectively. Poly (3,4-ethylenedioxythiophene) doped with poly (4-styrenesulfonate) (PEDOT:PSS) has frequently been used as a buffer material between the donor and ITO, while bathocuproine (BCP) has been used as a buffer material between the acceptor and electrode.<sup>9</sup> However, since we previously found from cross-sectional scanning electron

<sup>a)</sup>Author to whom correspondence should be addressed: j-onoe@energy.nagoya-u.ac.jp. Tel./Fax: +81-52-789-3784.

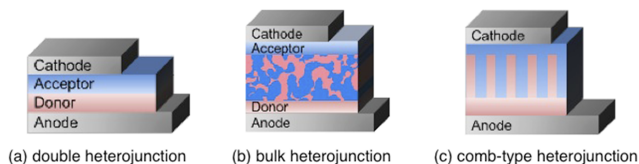


FIG. 1. Schematic diagrams of typical organic solar cells with (a) double heterojunction, (b) bulk heterojunction, and (c) comb-type heterojunction.

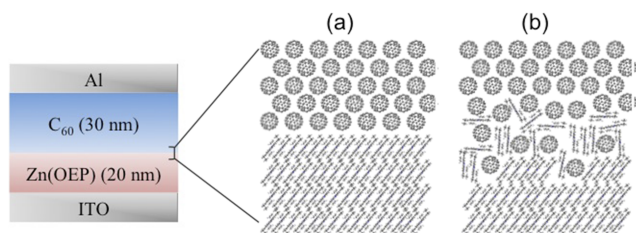


FIG. 2. Schematic illustration of the interfacial structure between Zn(OEP) and C<sub>60</sub> films at the molecular level: (a) atomically flat structure at the interface and (b) atomically mixed structure at the interface.

microscopy images that Zn(OEP) molecules are incorporated into PEDOT:PSS films,<sup>10</sup> we did not use these buffer materials from the viewpoint of obtaining OSCs with well-defined structures. Furthermore, we obtained a maximum external quantum efficiency of 42% for the [ITO/Zn(OEP)/C<sub>60</sub>/Al] OSC at an excitation wavelength of 400 nm,<sup>11</sup> which is higher than that (ca. 35%) for OSCs using the buffer materials.<sup>12</sup>

Among the elementary processes responsible for photoconversion current in OSCs, it is especially important to understand the D–A interactions that cause the exciton dissociation to generate carriers (electrons and holes) at the D/A interface. Figure 2(a) shows the ideal D/A interfacial structure of a double heterojunction at the molecular level. However, in a real system, it is assumed that the D and A molecules are randomly mixed on the molecular scale [Fig. 2(b)] because it is experimentally difficult both to form an atomically flat surface of a donor film on ITO (with no atomically flat surfaces commercially available) and to make C<sub>60</sub> gently adhere to the surface of the D film (kinetic energy is regarded as the driving force for incorporation into D films in the case of the thermal evaporation under vacuum conditions).

In the present study, we investigated the structural, electronic, and optical properties of the D/A mixed structure shown in Fig. 2(b), which may be typically formed in the vicinity of

the D/A interface, to achieve a better understanding of the D–A interactions that give rise to the dissociation of photogenerated excitons, using Fourier-transform infrared (FT-IR) spectroscopy, X-ray diffraction (XRD), ultraviolet-visible (UV-vis) absorption spectroscopy, and photoluminescence (PL) spectroscopy, in combination with first-principles and semi-empirical calculations (Gaussian09 package). Although there have been some reports on the interactions between Zn(OEP) and C<sub>60</sub> based on the examination of the Zn(OEP)–C<sub>60</sub> crystal structure formed in solution,<sup>13,14</sup> the inclusion of contaminants such as solvents was not avoided and the stoichiometric ratio between Zn(OEP) and C<sub>60</sub> was spontaneously determined by the crystallization requirements (specifically, the mixing ratio could not be controlled).

## II. EXPERIMENTS AND THEORETICAL CALCULATIONS

### A. Experiments

Figure 3 shows a schematic diagram of the apparatus used in this study, which consisted of an ultrahigh-vacuum (UHV) system (base pressure:  $3.0 \times 10^{-6}$  Pa), an FT-IR spectrometer (resolution:  $0.5 \text{ cm}^{-1}$ ), and two Knudsen cells, respectively, used for the thermal evaporation of C<sub>60</sub> and Zn(OEP). This system allowed us to measure the *in situ* FT-IR spectra of the molecules in the film. The IR optical paths out of the UHV chamber were purged with nitrogen (N<sub>2</sub>) gas (purity: 99%) supplied by a N<sub>2</sub> generator to eliminate the IR-active gases H<sub>2</sub>O and CO<sub>2</sub> from the background of the IR spectra as much as possible. This procedure has been described in detail elsewhere.<sup>15</sup>

For the preparation of the C<sub>60</sub> and Zn(OEP) films, C<sub>60</sub> (purity: 99.98%) and Zn(OEP) (purity: 98%) powders were placed into individual quartz crucibles. Subsequently, C<sub>60</sub> and Zn(OEP) were thermally evaporated at 673 K (deposition rate: 10 nm/min) and at 443 K (deposition rate: 1.1 nm/min), respectively, and deposited on double-sided polished Si(100) and quartz substrates. For the formation of Zn(OEP)/C<sub>60</sub> co-deposited films, we controlled the proportion of C<sub>60</sub> by varying the deposition rate of C<sub>60</sub> at a moderate temperature with a constant deposition of Zn(OEP) at 443 K. For example, when C<sub>60</sub> and Zn(OEP) were thermally evaporated at 623 K (deposition rate: 1.1 nm/min) and at 443 K, respectively, a Zn(OEP)/C<sub>60</sub> co-deposited film with the mixing ratio Zn(OEP):C<sub>60</sub> of 1:1 was formed on the substrates. The films

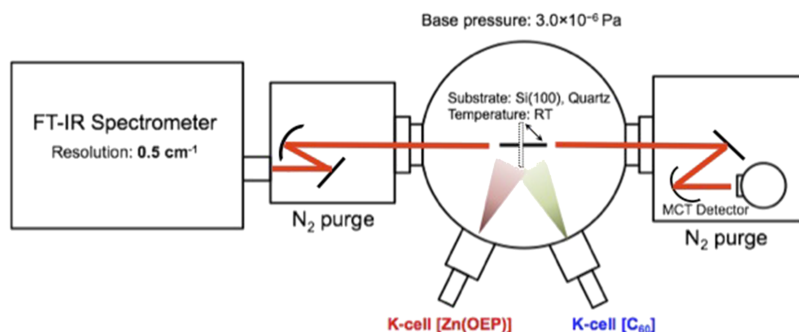


FIG. 3. Schematic diagram of the apparatus used in this study, consisting of an ultrahigh-vacuum system, an *in situ* Fourier-transform infrared spectrometer (FT-IR), Knudsen cells (K-cells) for the evaporation of Zn(OEP) and C<sub>60</sub>, and N<sub>2</sub> purge boxes for removing the IR active gases such as H<sub>2</sub>O and CO<sub>2</sub> present in atmospheric air from the IR optical path.

formed on the Si substrate were used to measure both the FT-IR spectra (resolution:  $0.5\text{ cm}^{-1}$ ) and PL spectra (resolution:  $0.2\text{ nm}$ ), whereas those on the quartz substrate were used to measure both the XRD pattern ( $\text{CuK}\alpha$ :  $1.5418\text{ \AA}$  and step scan:  $0.02^\circ$ ) and UV-vis absorption spectra (resolution:  $0.5\text{ nm}$ ). Prior to their deposition on the substrates, the Zn(OEP) and  $\text{C}_{60}$  powders in the crucibles were preheated at  $373\text{ K}$  and  $473\text{ K}$ , respectively, to remove residual solvents. The XRD, UV-vis, and PL results for the films described above were obtained *ex situ* after the removal of the films from the UHV chamber.

## B. Theoretical calculations

All of the calculations in the present study were performed using Gaussian09.<sup>16</sup> The  $\text{C}_{60}$  and Zn(OEP) molecules were geometrically optimized using density functional theory (DFT) calculations, where the def2-TZVP basis set was used for all of the atoms of the molecules<sup>17</sup> and the long-range corrected B3LYP (CAM-B3LYP) was used as the exchange-correlation potential.<sup>18</sup> The wavenumbers of the IR peaks for the optimized structure of the Zn(OEP) molecule were calculated using the coupled perturbed Hartree-Fock method.<sup>19</sup> To obtain the theoretical UV-vis absorption spectra of the Zn(OEP)- $\text{C}_{60}$  coordination system, the intermolecular distance ( $d$ ) between  $\text{C}_{60}$  and Zn(OEP) was estimated using the DFT+D method.<sup>20</sup> The dispersion interaction between the  $\text{C}_{60}$  and Zn(OEP) molecules was also taken into account by employing the Grimme-Dispersion-3 (GD3) method.<sup>20</sup> The binding energies of the two Zn(OEP)- $\text{C}_{60}$  coordination models (Fig. 7) were evaluated as a function of the intermolecular distance  $d$ . The UV-vis oscillator strengths of the most stable Zn(OEP)- $\text{C}_{60}$  coordination system were evaluated using the ZINDO (Zerner's intermediate neglect of differential overlap) method.<sup>21</sup> In the present calculations, 100 singlet excited states were considered because we have confirmed that this is sufficient for calculating the excitation energies of the molecular orbitals (MOs) of Zn(OEP) and  $\text{C}_{60}$ . Theoretical UV-vis absorption spectra were obtained using the convolution of the oscillator strength replaced by a Gaussian function with a full width at half maximum of  $1316\text{ cm}^{-1}$  ( $0.163\text{ eV}$ ). Since UV-vis absorption spectra of porphyrins have been understood in terms of the four frontier orbital (HOMO-1, HOMO, LUMO, and LUMO+1) model proposed by Gouterman,<sup>22-24</sup> we also basically focused on the four orbitals. The solvent effects on the MOs of Zn(OEP) and  $\text{C}_{60}$  were taken into account using the polarizable continuum model based on the integral equation formalism variant (IEFPCM)<sup>25</sup> with several different dielectric constants.

## III. RESULTS AND DISCUSSION

Figure 4(A) presents the FT-IR spectra of (a) a pristine  $\text{C}_{60}$  film ( $200\text{ nm}$  thick), (b) a pristine Zn(OEP) film ( $500\text{ nm}$  thick), and (c) a Zn(OEP)/ $\text{C}_{60}$  co-deposited film ( $1000\text{ nm}$  thick). The inset shows the magnified spectra (a)–(c) in the range of  $1400\text{--}1500\text{ cm}^{-1}$ . It can be seen upon comparing these FT-IR spectra that the overall appearance of spectrum (c) is essentially a superimposition of spectra (a) and (b). However, the inset reveals the presence of a new IR peak at  $1446\text{ cm}^{-1}$

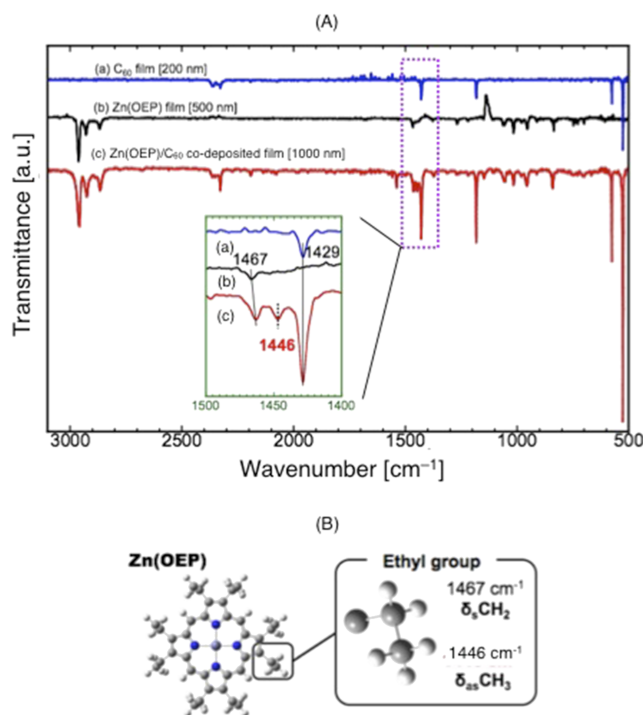


FIG. 4. (A) IR spectra of a pristine  $\text{C}_{60}$  film (a), a pristine Zn(OEP) film (b), and a Zn(OEP)/ $\text{C}_{60}$  co-deposited film (c), along with a magnified view of the  $1400\text{--}1500\text{ cm}^{-1}$  region (inset). (B) Schematic illustration of the structure of Zn(OEP) with a close-up view of an ethyl group showing the IR vibration wavenumbers of individual  $\text{CH}_2$  and  $\text{CH}_3$  groups.

only for the co-deposited film. Figure 4(B) shows the molecular structure of Zn(OEP), with the magnified ethyl ( $\text{C}_2\text{H}_5$ ) group exhibiting the IR vibrational modes at  $1467\text{ cm}^{-1}$  for  $\text{CH}_2$  and at  $1446\text{ cm}^{-1}$  for  $\text{CH}_3$ , according to the DFT calculations. In addition, the IR peak appearing at  $1429\text{ cm}^{-1}$  was ascribed to the in-plane (tangential) motion of  $\text{C}_{60}$ .<sup>26</sup> In an attempt to clarify why no IR peak corresponding to the  $\text{CH}_3$  of the ethyl group was observed for the Zn(OEP) film itself, we next compared the structural properties of pristine Zn(OEP) and Zn(OEP)/ $\text{C}_{60}$  co-deposited films.

Figure 5(a) shows the XRD patterns of pristine Zn(OEP) (red) and Zn(OEP)/ $\text{C}_{60}$  co-deposited (black) films formed on quartz substrates, alongside schematic representations of the crystal structure of Zn(OEP) [Fig. 5(b)] and Zn(OEP)/ $\text{C}_{60}$  [Fig. 5(c)]. As shown in Fig. 5(a), the pristine Zn(OEP) film was found to be crystalline with a grain size of  $60\text{--}70\text{ nm}$  estimated from the Scherrer equation and a shape factor of  $0.94$ ,<sup>27</sup> whereas the co-deposited film was amorphous. We previously investigated the crystal structure and molecular orientation of Zn(OEP) films on ITO and  $\text{SiO}_2/\text{Si}$  substrates using XRD and IR multiple-angle incidence resolution spectroscopy and found that Zn(OEP) films possess a crystal structure with molecular orientation aligned by ca.  $50^\circ$  on the substrates.<sup>28</sup> Since there are no significant differences in the surface features of quartz and  $\text{SiO}_2/\text{Si}$  substrates toward Zn(OEP) molecules, the crystal structures of Zn(OEP) films on the two surfaces should be similar [Fig. 5(b)]. In the crystalline film, the  $\text{CH}_3$  moiety in the ethyl group of Zn(OEP) is located close to the  $\text{CH}_2$  in an adjacent Zn(OEP) molecule, with a distance estimated to be  $2.4\text{ \AA}$  from the crystal structure. Such a short distance suggests

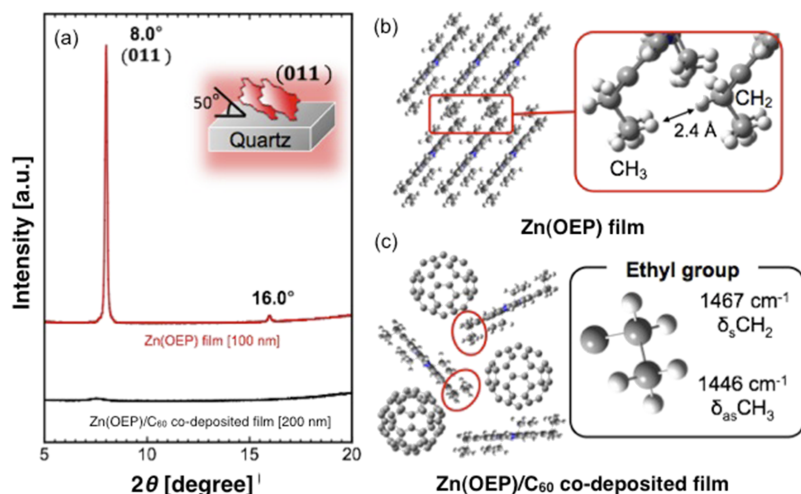


FIG. 5. (a) X-ray diffraction patterns of pristine Zn(OEP) (red) and Zn(OEP)/C<sub>60</sub> co-deposited (black) films and schematic illustrations of (b) Zn(OEP) crystal structure and (c) Zn(OEP)/C<sub>60</sub> mixed structure.

that the asymmetric vibration of CH<sub>3</sub> would be hindered by the interaction with the neighboring CH<sub>2</sub>, preventing us from observing the IR peak at 1446 cm<sup>-1</sup> for the Zn(OEP) crystalline film. On the contrary, in the amorphous Zn(OEP)/C<sub>60</sub> co-deposited film, the Zn(OEP) molecules are separated from each other by the C<sub>60</sub>, suggesting that no interactions can occur between the CH<sub>3</sub> and CH<sub>2</sub> moieties of the C<sub>2</sub>H<sub>5</sub> groups of adjacent Zn(OEP) molecules. Thus, the IR peak attributed to the CH<sub>3</sub> of the C<sub>2</sub>H<sub>5</sub> group could be observed at 1446 cm<sup>-1</sup>. Consequently, the FT-IR and XRD results for the co-deposited films indicate that the Zn(OEP) and C<sub>60</sub> molecules were mixed with each other on the molecular scale, as shown in Fig. 2(b).

We next examined the UV–vis spectra of Zn(OEP)/C<sub>60</sub> co-deposited films by varying the mixing ratio to Zn(OEP):C<sub>60</sub>. Figure 6(a) shows the overall UV–vis spectral changes of the Zn(OEP)/C<sub>60</sub> co-deposited films at various Zn(OEP):C<sub>60</sub> mixing ratios, and Fig. 6(b) shows the dependence of the positions of each of the four key peaks (a–d) on the proportion of C<sub>60</sub> in the co-deposited films. The insets show the magnifications of the spectrum of the co-deposited film with a Zn(OEP):C<sub>60</sub> ratio of 43:57 in the 340–500 nm and 550–600 nm regions.

The peak appearing in the former region was attributed to C<sub>60</sub>, whereas the peak appearing in the latter region was recognized as peak c. Unfortunately, peak b was buried in the C<sub>60</sub> absorption band. In the spectrum of the pristine Zn(OEP) film at the top of Fig. 6(a), peak a was assigned to the Soret band originating from the electron excitations between the HOMO-1 and LUMO (and LUMO+1). Since the ZINDO calculations show that the energy difference between the LUMO and LUMO+1 was only 4 meV for Zn(OEP), we regarded these two MOs as one degenerate MO in the present study [LUMO+1 was omitted in Figs. 9(a) and 10(b)]. On the other hand, peaks b and c also were assigned to the Q-band originating from the electron excitations between the HOMO and LUMO (and LUMO+1). In contrast, for the spectrum of the pristine C<sub>60</sub> film at the bottom of Fig. 6(a), the analysis of the calculation results revealed that peak d originates from the electron excitation between the HOMO and LUMO+1.

We next examined the line shifts of the four peaks a–d with respect to the Zn(OEP):C<sub>60</sub> mixing ratio. Figure 6(b) shows a plot of the peak positions as a function of the mixing ratio. Peak a exhibited a red shift, whereas both peaks b and c exhibited blue shifts. In contrast, peak d appeared to be

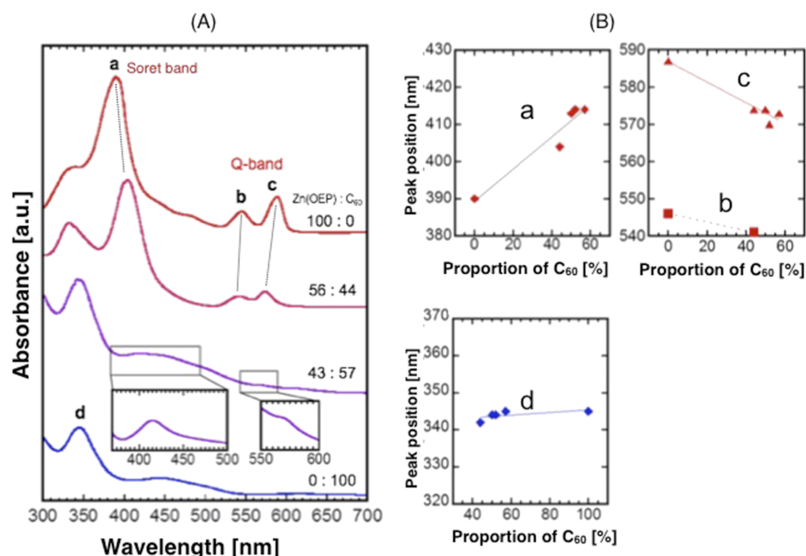


FIG. 6. (a) Typical UV–vis spectra of Zn(OEP)/C<sub>60</sub> co-deposited films with respect to various mixing ratios to Zn(OEP):C<sub>60</sub> and (b) the dependence of each peak (a–d) position on the mixing ratio.

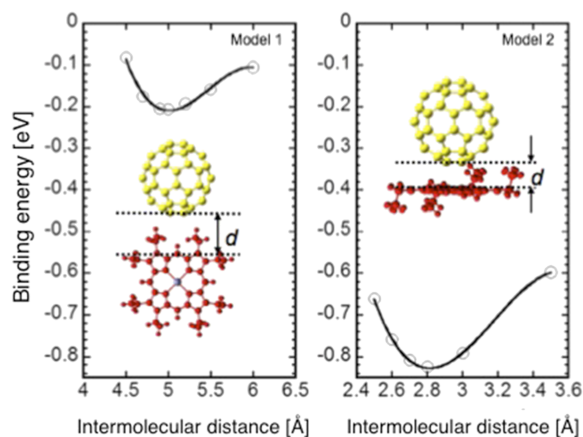


FIG. 7. Binding energies for the interaction between Zn(OEP) and  $C_{60}$  in model 1 (left) and model 2 (right).

independent of the mixing ratio. To understand this behavior, two representative coordination models between the Zn(OEP) and  $C_{60}$  molecules were considered. In model 1, Zn(OEP) is coordinated equatorially with  $C_{60}$ , whereas in model 2 it is coordinated facially. Figure 7 shows the binding energies ( $E_B$ ) of model 1 (left) and model 2 (right) as a function of the Zn(OEP)– $C_{60}$  intermolecular distance ( $d$ ), which was defined as shown in the inset. The lowest values of  $E_B$  for models 1 and 2 were found to occur when  $d$  was 5.0 Å and 2.8 Å, respectively. Since the difference in  $E_B$  between the two models was determined to be 0.6 eV, the abundance ratio (model 2/model 1) was estimated as  $1.4 \times 10^{10}$  using the Boltzmann

distribution function. This allows us to consider only model 2 for understanding the line shifts of the four peaks **a–d** with respect to the Zn(OEP): $C_{60}$  mixing ratio, which is consistent with theoretical results reported previously.<sup>29</sup>

Figure 8 shows (i) a schematic illustration of several coordination structures based on model 2, (ii) the calculated UV–vis spectra (red) along with the oscillator strengths (blue) for each corresponding coordination structure, and (iii) the line shifts of each peak (**a**, **b**, and **d**) with respect to the proportion of  $C_{60}$ . Since the ZINDO calculations underestimated the energy difference (4 meV) between the LUMO and LUMO+1 of Zn(OEP), peaks **b** and **c**, which were observed separately in Fig. 6(a), could not be distinguished from each other and occur as one single peak in the theoretical Q-band shown in Fig. 8(a). However, since both peaks would be expected to exhibit similar line shifts, it is reasonable to examine the line shifts of peaks **a**, **b**, and **d** as a function of the Zn(OEP): $C_{60}$  mixing ratio. From the results in Fig. 8(b) showing the positions of peaks **a**, **b**, and **d**, in Fig. 8(c), the line shifts of these peaks are presented with respect to the Zn(OEP): $C_{60}$  mixing ratio. In terms of the proportion of  $C_{60}$  in the films, the structures labeled as A, B, and C in Fig. 8(a) correspond to 33%, 50%, and 66%, respectively, where pristine  $C_{60}$  and Zn(OEP) films represent 100% and 0%, respectively. As shown in Fig. 8(c), there was agreement in the line shift behavior between the experimental and theoretical results for peaks **a** and **d**. In contrast, peak **b** exhibited a red shift with respect to the proportion of  $C_{60}$ , which is the opposite trend to that observed in the experimental results presented in Fig. 6(b). This discrepancy may be due to the solvent effects of  $C_{60}$  not

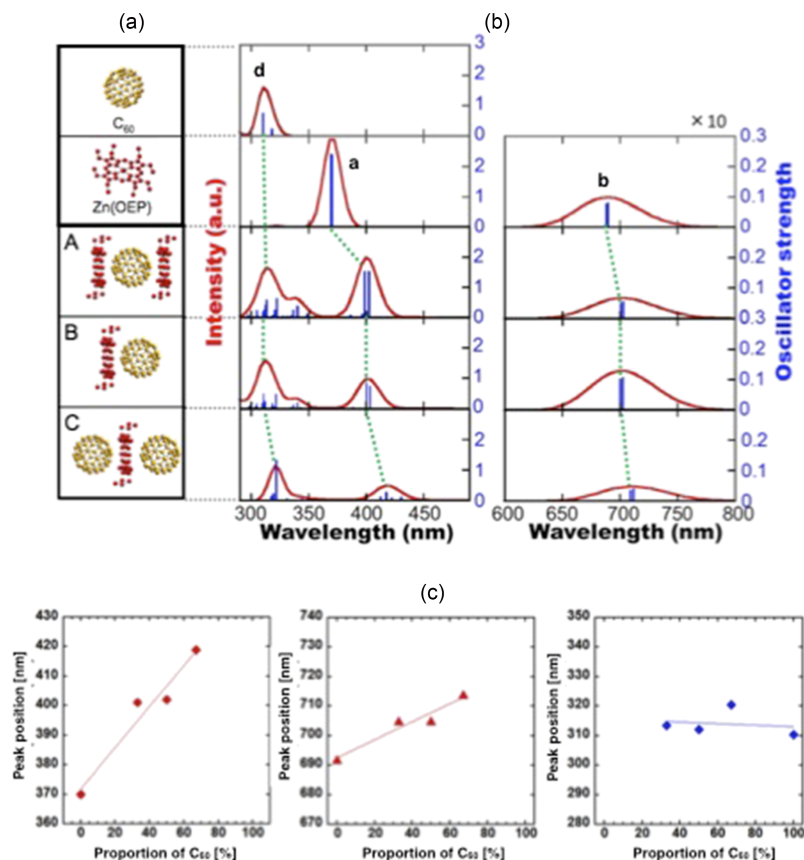


FIG. 8. (a) Model structures corresponding to each of the calculated UV–vis spectra shown in (b), (b) calculated UV–vis spectra (red) along with the oscillator strengths (blue) for each of the models, and (c) the line shifts of each peak (**a**, **b**, and **d**) versus the proportion of  $C_{60}$ .

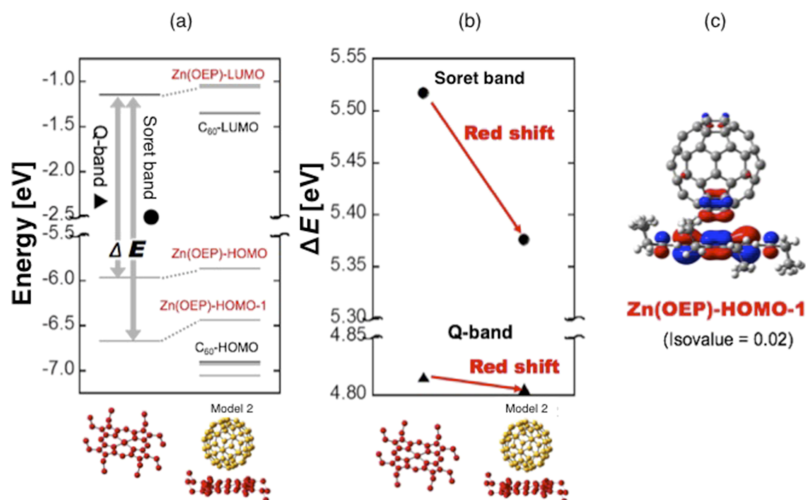


FIG. 9. (a) Energy level diagram of the molecular orbitals (MOs) for Zn(OEP) (left) and Zn(OEP)/C<sub>60</sub> (right), (b) changes in the excitation energies of the Soret and Q-bands of Zn(OEP) before and after the interaction with C<sub>60</sub>, and (c) the wave function of the HOMO-1 of Zn(OEP) for model 2.

being considered in the calculations, which will be discussed later. To first explain the red shift of peak **a** corresponding to the Soret band, we next examined the energy level diagram for the MOs of Zn(OEP) before and after the interaction with C<sub>60</sub>.

Figure 9 shows (a) the energy level diagram for the MOs of Zn(OEP) before (left) and after (right) the interaction with C<sub>60</sub>, (b) the changes in the excitation energies of the Soret band and Q-bands of Zn(OEP) before and after the interaction, and (c) a schematic illustration of the HOMO-1 wave function of Zn(OEP). It can be seen from Fig. 9(a) that the LUMO, HOMO, and HOMO-1 all shift toward higher energies after the coordination with C<sub>60</sub>. Correspondingly, the energy differences between both the LUMO and HOMO (Q-band) and the LUMO and HOMO-1 (Soret band) become small compared to those before the interaction, which results in the red shift of not only peak **a** but also peak **b** [Fig. 9(b)]. In particular, the HOMO-1 is significantly affected by the interaction with C<sub>60</sub> because the MO becomes spread over a portion of C<sub>60</sub> as shown in Fig. 9(c). However, the natural bond orbital analysis<sup>30</sup> indicated that the charge transfer from Zn(OEP) to C<sub>60</sub> involves only 0.008 electrons, which may be negligible. In contrast, we confirmed that the MOs of C<sub>60</sub> remain almost unchanged before and after the interaction with Zn(OEP), thus resulting in the independence of peak **d** from the proportion of C<sub>60</sub>.

We next discuss the discrepancy in the line shift of peak **b** between the experimental and theoretical results. As described above, the solvent effects of C<sub>60</sub> were not considered for the results shown in Fig. 9(a), despite the increasing proportion of C<sub>60</sub>. Figure 10 shows (a) a schematic illustration of the C<sub>60</sub>-based solvent effects on Zn(OEP); (b) the MO energy level diagram of Zn(OEP) (left) together with a revised version of model 2 after consideration of the solvent effects of diethyl ether, whose dielectric constant of 4.34<sup>31</sup> is close to that of C<sub>60</sub> (4.4<sup>32</sup>) (right), which was necessary because Gaussian09 does not allow the solvent effects of C<sub>60</sub> to be considered directly; and (c) the changes in the excitation energies of the Soret and Q-bands of Zn(OEP) before and after the interaction with C<sub>60</sub>. As shown in Fig. 10(a), since the number of C<sub>60</sub> molecules surrounding one Zn(OEP) molecule increases with the proportion of C<sub>60</sub>, Zn(OEP) can be ultimately regarded as a solute in the C<sub>60</sub> solvent. This implies that the solvent effects of C<sub>60</sub> become significant upon increasing the proportion of C<sub>60</sub>. We thus re-examined the energy level diagram for model 2 with consideration of the solvent effects. A comparison between the energy level diagrams shown in Figs. 9(a) and 10(b) revealed that the LUMO, HOMO, and HOMO-1 of Zn(OEP) all shift toward lower energies, which is the opposite phenomenon to that observed without the solvent effects. This indicates that the MOs become more stable as a result of the solvent effects. From the energy differences of the Soret and Q-bands, it can

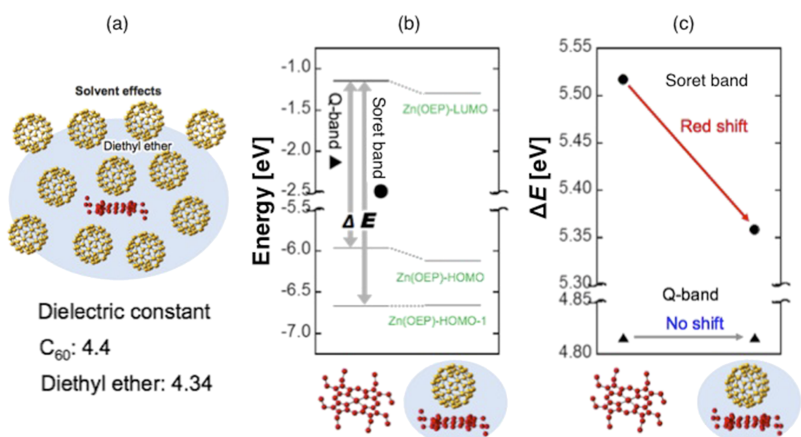


FIG. 10. (a) Schematic illustration of the solvent effects of C<sub>60</sub> on Zn(OEP), (b) MO energy diagram of Zn(OEP) (left) and model 2 after considering the solvent effects of diethyl ether with a dielectric constant (4.34) close to that (4.4) of C<sub>60</sub> (right), and (c) changes in the excitation energies of the Soret and Q-bands of Zn(OEP) before and after the interaction with C<sub>60</sub> after considering the solvent effects.

be deduced from Fig. 10(c) that peak **a** still exhibits a red shift in a similar manner to the experimental result, whereas peak **b** exhibits not a red shift but almost no shift. The reason behind the underestimated excitation energy for peak **b** cannot be clearly understood at present, but it presumably arises because the present calculations did not consider the anisotropic solvent effects. As shown in Fig. 10(a), the Zn(OEP) molecule is assumed to be affected by the isotropic solvent effects of C<sub>60</sub>, but it is surrounded by C<sub>60</sub> molecules anisotropically, according to the coordination model depicted in Fig. 7. If the anisotropic solvent effects of C<sub>60</sub> are considered in the MO calculations, the individual MO energy levels could be estimated more precisely. This will be the subject of a future study.

To confirm that electron transfer takes place from Zn(OEP) to C<sub>60</sub>, we examined the PL spectrum (the transition from the singlet excited state, S<sub>1</sub>, to the singlet ground state, S<sub>0</sub>) of the Zn(OEP)/C<sub>60</sub> co-deposited film, which is regarded as the D/A interfacial region of heterojunction OSCs (Fig. 2), along with that of the pristine Zn(OEP) film. The excitation wavelength was set to the peak position of the Soret band at 390 nm for the pristine Zn(OEP) film and to 404 nm for the Zn(OEP)/C<sub>60</sub> co-deposited film, respectively. Figure 11 shows (a) the PL spectra of the Zn(OEP) (black) and Zn(OEP)/C<sub>60</sub> co-deposited (red) films and (b) the MO energy level diagram of Zn(OEP) where S<sub>0</sub> has two levels as a result of the vibronic interactions (Jablonski diagram),<sup>33–35</sup> which correspond to PL peaks **a** and **b** at 594 and 636 nm, respectively. The Zn(OEP) film exhibited two PL peaks **a** and **b**, which originated from the photo-excited electron dynamics shown in Fig. 11(b), whereas no such PL peaks were observed for the Zn(OEP)/C<sub>60</sub> co-deposited film. This clearly demonstrates that the photo-excited electron immediately transfers from Zn(OEP) to C<sub>60</sub>, which inhibits the PL observed for the Zn(OEP) film itself.

The results obtained in the present work lead us to conclude that the D/A mixing layers formed in the interfacial region play a crucial role on completely dissolving the photogenerated excitons to generate the electrons and holes that cause the short-circuit current relevant to the  $\eta$  of OSCs. This

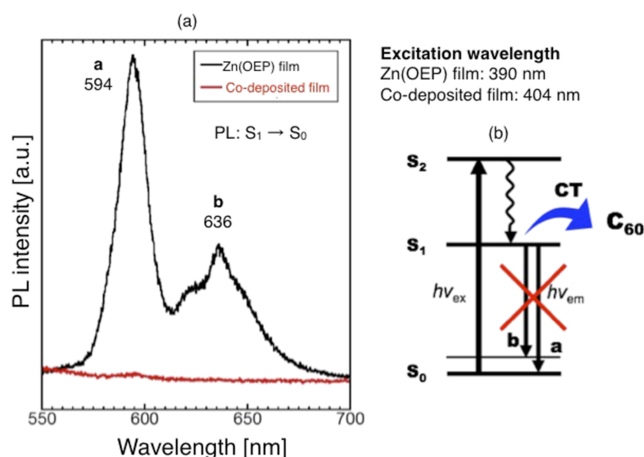


FIG. 11. (a) Photoluminescence ( $S_1 \rightarrow S_0$ ) of pristine Zn(OEP) (black) and Zn(OEP)/C<sub>60</sub> co-deposited (red) films and (b) schematic MO energy level diagram of Zn(OEP) for the S<sub>0</sub> state with two levels caused by the vibronic interactions (Jablonski diagram), which correspond to the peak **a** at 594 nm and peak **b** at 636 nm in the PL spectrum.

finding is useful for understanding OSCs with any of the D/A heterojunctions shown in Fig. 1.

#### IV. SUMMARY

We have investigated the Zn(OEP)/C<sub>60</sub> co-deposited films with various mixing ratios using FT-IR, XRD, UV-vis, and PL measurements in combination with the first-principles and semi-empirical calculations to elucidate the structural, electronic, and optical properties of the Zn(OEP)/C<sub>60</sub> interfacial region formed in OSCs. The UV-vis spectral changes in the Soret and Q-bands of Zn(OEP), with respect to the proportion of C<sub>60</sub> could be well explained by the model in which Zn(OEP) interacts with C<sub>60</sub> in a face-to-face manner with consideration of the C<sub>60</sub> solvent effects. Analysis of the MO levels revealed that the LUMO (and LUMO+1), HOMO, and HOMO-1 were significantly affected by the interaction with C<sub>60</sub>, and in particular, the HOMO-1 wave function were found to spread over a portion of C<sub>60</sub>. Since no PL peaks ( $S_1 \rightarrow S_0$ ) from the excited Soret band of Zn(OEP) were observed for the co-deposited films, the D/A mixing layers play a crucial role in dissolving the photogenerated excitons to generate carriers (electrons and holes), thereby providing the short-circuit current that is relevant to the energy conversion efficiency of the OSCs.

#### ACKNOWLEDGMENTS

We are grateful to Dr. M. Yoshino and Professor T. Nagasaki at Nagoya University for the XRD and PL measurements. The present work was supported in part by the Japan-France Research Cooperative Program between JSPS (Japan Society for the Promotion of Science) and CNRS (Centre National de la Recherche Scientifique).

<sup>1</sup>For example: *Organic Solar Cells: Materials, Devices, Interfaces, and Modeling*, edited by Q. Qiao (CRC Press, New York, 2015).

<sup>2</sup>P. Peumans, A. Yakimov, and S. R. Forrest, *J. Appl. Phys.* **93**, 3693 (2003).

<sup>3</sup>M. C. Scharber and N. S. Sariciftci, *Prog. Polym. Sci.* **38**, 1929 (2013).

<sup>4</sup>A. Slaoui and R. T. Collins, *MRS Bull.* **32**, 211 (2007).

<sup>5</sup>S. Ryuzaki and J. Onoe, *Nano Rev.* **4**, 21055 (2013).

<sup>6</sup>C. W. Tang, *Appl. Phys. Lett.* **48**, 183 (1986).

<sup>7</sup>C. Müller, T. A. M. Ferenczi, M. Campoy-Quiles, J. M. Frost, D. D. C. Bradley, P. Smith, N. Stingelin-Stutzmann, and J. Nelson, *Adv. Mater.* **20**, 3510 (2008).

<sup>8</sup>P. K. Watkins, A. B. Walker, and G. L. B. Vershoor, *Nano Lett.* **5**, 1814 (2005).

<sup>9</sup>A. B. Djurisic and C. Y. Kwong, *Organic Photovoltaics: Mechanisms, Materials, and Devices*, edited by S.-S. Sun and N. S. Sariciftci (CRC Press, New York, 2005), Chap. 20, p. 453.

<sup>10</sup>S. Ryuzaki and J. Onoe, *J. Appl. Phys.* **106**, 023526 (2009).

<sup>11</sup>S. Ryuzaki, T. Kai, Y. Toda, S. Adachi, and J. Onoe, *J. Phys. D: Appl. Phys.* **44**, 145103 (2011).

<sup>12</sup>P. Peumans and S. R. Forrest, *Appl. Phys. Lett.* **79**, 126 (2001).

<sup>13</sup>M. M. Olmstead, D. A. Costa, K. Maitra, B. C. Noll, S. L. Phillips, P. M. Van Calcar, and A. L. Balch, *J. Am. Chem. Soc.* **121**, 7090 (1999).

<sup>14</sup>D. V. Konarev, S. S. Khasanov, G. Saito, and R. N. Lyubovskaya, *Cryst. Growth Des.* **9**, 1170 (2009).

<sup>15</sup>J. Onoe and K. Takeuchi, *J. Phys. Chem.* **99**, 16786 (1995).

<sup>16</sup>M. J. Frisch, G. W. Trucks, H. B. Schlegel, G. E. Scuseria, M. A. Robb, J. R. Cheeseman, G. Scalmani, V. Barone, G. A. Petersson, H. Nakatsuji, X. Li, M. Caricato, A. Marenich, J. Bloino, B. G. Janesko, R. Gomperts, B. Mennucci, H. P. Hratchian, J. V. Ortiz, A. F. Izmaylov, J. L. Sonnenberg, D. Williams-Young, F. Ding, F. Lipparini, F. Egidi, J. Goings, B. Peng, A. Petrone, T. Henderson, D. Ranasinghe, V. G. Zakrzewski, J. Gao, N. Rega, G. Zheng, W. Liang, M. Hada, M. Ehara, K. Toyota, R. Fukuda, J. Hasegawa, M. Ishida, T. Nakajima, Y. Honda, O. Kitao, H. Nakai,

- T. Vreven, K. Throssell, J. A. Montgomery, Jr., J. E. Peralta, F. Ogliaro, M. Bearpark, J. J. Heyd, E. Brothers, K. N. Kudin, V. N. Staroverov, T. Keith, R. Kobayashi, J. Normand, K. Raghavachari, A. Rendell, J. C. Burant, S. S. Iyengar, J. Tomasi, M. Cossi, J. M. Millam, M. Klene, C. Adamo, R. Cammi, J. W. Ochterski, R. L. Martin, K. Morokuma, O. Farkas, J. B. Foresman, and D. J. Fox, *GAUSSIAN 09*, Revision D.01, Gaussian, Inc., Wallingford, CT, 2013.
- <sup>17</sup>F. Weigend and R. Ahlrichs, *Phys. Chem. Chem. Phys.* **7**, 3297 (2005).
- <sup>18</sup>T. Yanai, D. P. Tew, and N. C. Handy, *Chem. Phys. Lett.* **393**, 51 (2004).
- <sup>19</sup>R. McWeeny, *Rev. Mod. Phys.* **32**, 335 (1960).
- <sup>20</sup>S. Grimme, J. Antony, S. Ehrlich, and S. Krieg, *J. Chem. Phys.* **132**, 154104 (2010).
- <sup>21</sup>M. C. Zerner, *Rev. Comput. Chem.* **2**, 313 (1991).
- <sup>22</sup>M. Gouterman, *J. Chem. Phys.* **30**, 1139 (1959).
- <sup>23</sup>M. Gouterman, *J. Mol. Spectrosc.* **6**, 138 (1961).
- <sup>24</sup>M. Gouterman, D. Holten, and E. Lieberman, *Chem. Phys.* **25**, 139 (1977).
- <sup>25</sup>J. Tomasi, B. Mennucci, and R. Cammi, *Chem. Rev.* **105**, 2999 (2005).
- <sup>26</sup>R. E. Stanton and M. D. Newton, *J. Phys. Chem.* **92**, 2141 (1988).
- <sup>27</sup>P. Scherrer, *Nachr. Ges. Wiss. Goettingen, Math-Phys. Kl.* **98** (1918), available at <https://www.digizeitschriften.de/dms/img/?PID=GDZPPN002505045>.
- <sup>28</sup>S. Ryuzaki, T. Hasegawa, and J. Onoe, *J. Appl. Phys.* **105**, 113529 (2009).
- <sup>29</sup>F. F. Contreras-Torres and V. A. Basiuk, in *DFT Calculations on Fullerenes and Carbon Nanotubes*, edited by V. A. Basiuk and S. Irle (Research Signpost, Kerala, 2008), Chap. 12, p. 435 and references therein.
- <sup>30</sup>J. P. Foster and F. Weinhold, *J. Am. Chem. Soc.* **102**, 7211 (1980).
- <sup>31</sup>The value is included as a default one in the Gaussian09 package.
- <sup>32</sup>A. F. Hebard, R. C. Haddon, R. M. Fleming, and A. R. Kortan, *Appl. Phys. Lett.* **59**, 2109 (1991).
- <sup>33</sup>T. C. Van Cott, J. L. Rose, G. C. Misener, B. E. Williamson, A. E. Schrimpf, M. E. Boyle, and P. N. Schatz, *J. Phys. Chem.* **93**, 2999 (1989).
- <sup>34</sup>G. A. Peralta, M. Seth, and T. Ziegler, *Inorg. Chem.* **46**, 9111 (2007).
- <sup>35</sup>M. Guo, R. He, Y. Dai, W. Shen, M. Li, C. Zhu, and S. H. Lin, *J. Chem. Phys.* **136**, 144313 (2012).